Superexchange interactions between spin-orbit-coupled $j \approx 1/2$ ions in oxides with face-sharing ligand octahedra

Lei Xu,[1] Ravi Yadav,[1] Viktor Yushankhai,[2,3] Liudmila Siurakshina,[2] Jeroen van den Brink,[1,4,5] and Liviu Hozoi[1]

[1]*Institute for Theoretical Solid State Physics, IFW Dresden, Helmholtzstr. 20, 01069 Dresden, Germany*

[2]*Joint Institute for Nuclear Research, Joliot-Curie 6, 141980 Dubna, Russia*

[3]*Max-Planck-Institut für Physik komplexer Systeme, Nöthnitzerstr. 38, 01187 Dresden, Germany*

[4]*Department of Physics, Technical University Dresden, Helmholtzstr. 10, 01069 Dresden, Germany*

[5]*Department of Physics, Washington University, St. Louis, Missouri 63130, USA*

(Received 20 November 2018; revised manuscript received 24 January 2019; published 14 March 2019)

Using *ab initio* wave-function-based calculations, we provide valuable insights with regard to the magnetic exchange in 5*d* and 4*d* oxides with face-sharing ligand octahedra, $BaIrO_3$ and $BaRhO_3$. Surprisingly strong antiferromagnetic Heisenberg interactions as large as 400 meV are computed for idealized iridate structures with 90° Ir-O-Ir bond angles and in the range of 125 meV for angles of 80° as measured experimentally in $BaIrO_3$. These estimates exceed the values derived so far for corner-sharing and edge-sharing systems and motivate more detailed experimental investigations of quantum magnets with extended $5d/4d$ orbitals and networks of face-sharing ligand cages. The strong electron-lattice couplings evidenced by our calculations suggest rich phase diagrams as a function of strain and pressure, a research direction with much potential for materials of this type.

DOI: 10.1103/PhysRevB.99.115119

I. INTRODUCTION

The interest in the preparation and characterization of 5*d* oxides and halides goes back to the 1950's but some of the major implications of having a strong spin-orbit coupling (SOC), at least for certain $5d^n$ electron configurations, have been only recently realized. The work of Kim *et al.* on the square-lattice $5d^5$ iridate Sr_2IrO_4 [1,2], for example, led to the concept of a spin-orbit driven (Mott-like) insulator while Jackeli and Khaliullin [3] brought to the forefront of oxide research the honeycomb $5d^5$ iridates, as possible hosts for Kitaev physics [4] and novel magnetic ground states and excitations [5]. Both types of these iridate structures—square and honeycomb lattices—have been the topic of extensive investigations in recent years. The honeycomb compounds display edge-sharing ligand octahedra and advanced electronic-structure calculations indicate that the Kitaev exchange is indeed the largest intersite magnetic coupling [6,7]. Remarkably large anisotropic interactions were also found for corner-sharing ligand cages in Sr_2IrO_4, in that case of Dzyaloshinskii-Moriya type, with strengths in the range of 10–15 meV [3,8].

In contrast to the cases of corner- and edge-sharing coordination, little is known with respect to the magnitude of the effective coupling constants for adjacent octahedra connected through a O_3 facet. Representative materials of the latter type are the canted antiferromagnet $BaIrO_3$ [9–14], the putative spin-liquid $Ba_3InIr_2O_9$ [15], the spin-gapped system $Ba_3BiIr_2O_9$ [16], $BaRhO_3$ [17], and $BaCoO_3$ [18]. Here we provide *ab initio* results with regard to the strength of facet-mediated superexchange for IrO_6 (RhO_6) octahedra as found in the 5*d* (4*d*) t_{2g}^5 system $BaIrO_3$ ($BaRhO_3$). We predict remarkably large antiferromagnetic (AFM) Heisenberg interactions in the range of 100 meV for Ir-O-Ir angles of about 80° as found experimentally in $BaIrO_3$ [17]. Moreover, for bond angles $\gtrsim$85° the Heisenberg J even exceeds 200 meV in our simulations. So strong AFM superexchange has been found so far only in one-dimensional corner-sharing cuprates [19,20]. Our findings point to a picture of unusually large, AFM couplings within the face-sharing octahedral units of $BaIrO_3$. The strong dependence on bond angles of the effective magnetic interactions further resonates with available experimental data on $BaIrO_3$ [10,13,21–23] and $Ba_3BiIr_2O_3$ [16] that indicate subtle interplay between the electronic and lattice degrees of freedom.

II. MATERIAL MODEL

$BaIrO_3$ features a distorted hexagonal structure with both face-sharing and corner-sharing IrO_6 octahedra [24]. Those connected by one single ligand form honeycomb-like planes; the linkage of adjacent honeycomb layers is ensured by interlayer Ir ions located such that blocks of three face-sharing octahedra are formed along the *c* axis, see Fig. 1(a). Since for any pair of nearest-neighbor (NN) octahedra the actual point-group symmetry is very low, we focus in our study on an idealized material model displaying D_{3h} symmetry: $[Ir_2O_9]^{10-}$ units as depicted in Fig. 1(b) around which we additionally considered, for keeping overall charge neutrality, three Ba sites within the plane of the median O_3 facet and two extra Ba ions along the *z* axis. Although this material model is somewhat oversimplified, it should rather well describe the essential short-range electron interactions, as confirmed by similar investigations of edge-sharing $5d^5$ compounds [7].

One feature of 5*d* transition-metal (TM) ions is that their valence orbitals are much more diffuse as compared to first-series TM species. The ligand field is therefore more effectively felt and for instance the Ir^{4+} ions tend to adopt low-spin t_{2g}^5 configurations. The more extended nature of the

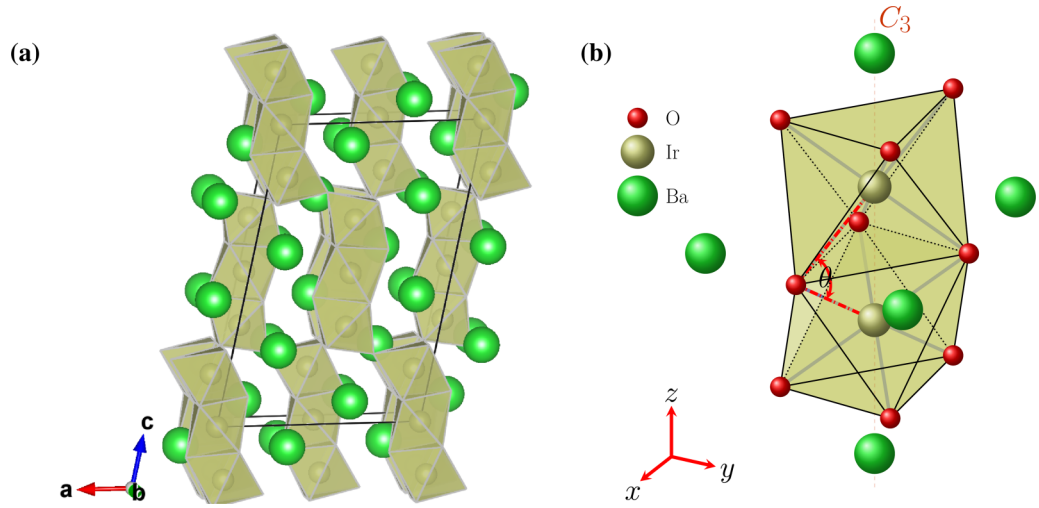

FIG. 1. (a) Crystal structure of $BaIrO_3$, with both face-sharing and corner-sharing IrO_6 octahedra. Ba atoms are shown as large green spheres. (b) Material model used for the calculation of magnetic interactions between two NN TM sites with face-sharing connectivity of the O octahedra. The point-group symmetry is D_{3h}.

$5d$ functions further gives rise to large intersite hoppings and large superexchange, as in, e.g., Sr_2IrO_4 [3,8] and $CaIrO_3$ [25].

Under strong octahedral crystal fields (CFs) and spin-orbit interactions, with one single unpaired electron ($S = 1/2$) in the t_{2g} manifold (orbital angular momentum $L = 1$), the $5d^5$ ($4d^5$) valence electron configuration of Ir^{4+} (Rh^{4+}) in $BaIrO_3$ ($BaRhO_3$) yields an effective $j = 1/2$ Kramers-doublet ground state [3,26]. Deviations from a perfect cubic environment may lead to some degree of admixture between the $j = 1/2$ and lower-lying $j = 3/2$ spin-orbit states [26]. In $BaIrO_3$ and $BaRhO_3$, in particular, the trigonal distortion of the oxygen octahedra plays a quite important role in this regard, as illustrated in Appendix A through simple analytical expressions based on an effective ionic model. To estimate the strengths of the exchange interactions in $BaIrO_3$ and $BaRhO_3$, both isotropic and anisotropic, we here employ many-body *ab initio* techniques from wave-function-based quantum chemistry (QC), then map the magnetic spectrum obtained in the QC calculations onto an appropriate effective spin Hamiltonian, the form of the latter being dictated by the symmetry of the material model.

III. MAGNETIC INTERACTIONS

For the idealized M_2O_9 cluster (M = Ir, Rh) of face-sharing octahedra [Fig. 1] the overall symmetry is D_{3h}. Each particular superexchange path M_i-O_n-M_j (n = 1,2,3) implies a finite Dzyaloshinskii-Moriya (DM) vector $\mathbf{D}^n_{ij}$, since there is no inversion center for the M_2O_9 unit. However, given the D_{3h} symmetry, these DM vectors lie within the plane of the O_3 facet and are related to each other through rotations around the C_3 axis. This yields a vanishing DM coupling $\mathbf{D}_{ij} = \sum_n \mathbf{D}^n_{ij} = 0$. For a pair of NN 1/2 pseudospins $\tilde{\mathbf{S}}_i$ and $\tilde{\mathbf{S}}_j$ with this type of linkage, the most general bilinear spin Hamiltonian can be then cast in the form

$$\mathcal{H}_{ij} = J_{ij}\tilde{\mathbf{S}}_i \cdot \tilde{\mathbf{S}}_j + \tilde{\mathbf{S}}_i \cdot \mathbf{\Gamma}_{ij} \cdot \tilde{\mathbf{S}}_j, \tag{1}$$

where J_{ij} is the isotropic Heisenberg exchange and $\mathbf{\Gamma}_{ij}$ is a symmetric traceless second-rank tensor that describes the symmetric exchange anisotropy. Considering the three-fold rotational symmetry around the M-M link, it is convenient to have one of the coordinates along the line defined by the two M sites. We therefore use the local frame indicated in Fig. 1, with both Ir ions on the z axis. In this coordinate system, the $\bar{\bar{\mathbf{\Gamma}}}$ tensor is diagonal and, for symmetry reasons, can be written as

$$\bar{\bar{\mathbf{\Gamma}}} = \begin{pmatrix} \Gamma & 0 & 0 \\ 0 & \Gamma & 0 \\ 0 & 0 & -2\Gamma \end{pmatrix}. \tag{2}$$

The eigenstates of such a two-site $\tilde{S} = 1/2$ system are the singlet $|\Psi_S\rangle = (|\uparrow\downarrow\rangle - |\downarrow\uparrow\rangle)/\sqrt{2}$ and the three triplet components $|\Psi_1\rangle = (|\uparrow\downarrow\rangle + |\downarrow\uparrow\rangle)/\sqrt{2}$, $|\Psi_2\rangle = (|\uparrow\uparrow\rangle + |\downarrow\downarrow\rangle)/\sqrt{2}$, $|\Psi_3\rangle = (|\uparrow\uparrow\rangle - |\downarrow\downarrow\rangle)/\sqrt{2}$. The corresponding eigenvalues are

$$E_S = -\tfrac{3}{4}J, \quad E_1 = \tfrac{1}{4}J - \tfrac{1}{2}\Gamma,$$
$$E_2 = \tfrac{1}{4}J + \Gamma, \quad E_3 = \tfrac{1}{4}J - \tfrac{1}{2}\Gamma. \tag{3}$$

Expression (1) can be then simplified to

$$\mathcal{H}_{ij} = \bar{J}\tilde{\mathbf{S}}_i \cdot \tilde{\mathbf{S}}_j + \bar{\Gamma}\tilde{S}^z_i\tilde{S}^z_j, \tag{4}$$

where $\bar{J} \equiv J + \Gamma$ and $\bar{\Gamma} \equiv -3\Gamma$.

The first step in the actual QC calculations is defining a relevant set of Slater determinants in the prior complete-active-space self-consistent-field (CASSCF) treatment [27]. For two IrO_6 (RhO_6) octahedra, an optimal choice is having five electrons and three (t_{2g}) orbitals at each of the two magnetically active Ir (Rh) sites. The self-consistent-field optimization was carried out for an average of the lowest nine singlet and lowest nine triplet states associated with this manifold. Subsequent multireference configuration-interaction (MRCI) computations were performed for each spin multiplicity, either singlet or triplet, as nine-root calculations. All these

TABLE I. Energy splittings for the lowest four spin-orbit states of two face-sharing NN IrO_6 octahedra and the corresponding effective coupling constants at different levels of approximation, for $d_0 = 2.63$ Å and $\theta_0 = 80^\circ$ (all values in meV). The J values without SOC by rAS, CAS, and CI are -1.2, 27.4, and 35.4 meV, respectively.

	rAS+SOC	CAS+SOC	CI+SOC
$\Psi_S = (\lvert\uparrow\downarrow\rangle - \lvert\downarrow\uparrow\rangle)/\sqrt{2}$	15.2	0.0	0.0
$\Psi_2 = (\lvert\uparrow\uparrow\rangle + \lvert\downarrow\downarrow\rangle)/\sqrt{2}$	0.4	72.0	123.3
$\Psi_3 = (\lvert\uparrow\uparrow\rangle - \lvert\downarrow\downarrow\rangle)/\sqrt{2}$	0.0	74.0	126.5
$\Psi_1 = (\lvert\uparrow\downarrow\rangle + \lvert\downarrow\uparrow\rangle)/\sqrt{2}$	0.0	74.0	126.5
$\bar{J}, \bar{\Gamma}$	$-14.9, -0.7$	72.0, 4.1	123.3, 6.3

TABLE II. Energy splittings for the lowest four spin-orbit states and the corresponding effective coupling constants for variable Ir-O-Ir angle, MRCI+SOC results (meV). The NN Ir-Ir distance is $d_0 = 2.63$ Å. The Ir-O-Ir angle θ is listed for each geometry; distances between Ir and the bridging O's, d(Ir-O), are provided within brackets.

	70.5°(2.27Å)	75°(2.16Å)	80°(2.04Å)	85°(1.94Å)	90°(1.86Å)
Ψ_S	0.0	0.0	0.0	0.0	0.0
Ψ_2	58.2	73.9	123.3	225.8	417.5
Ψ_1	73.4	81.8	126.5	226.9	418.5
Ψ_3	73.4	81.8	126.5	226.9	418.5
$\bar{J}, \bar{\Gamma}$	58.2, 30.3	73.9, 15.9	123.3, 6.3	225.8, 2.1	417.5, 2.0

states entered the spin-orbit treatment [28], in both CASSCF and MRCI. Within the group of 36 spin-orbit eigenvectors associated with the $t_{2g}^5 - t_{2g}^5$ manifold, the lowest-lying four "magnetic" states are separated by a significant energy gap from the other 32 states. The latter correspond to on-site $j \approx 3/2$ to $j \approx 1/2$ transitions, and are therefore left aside in the actual mapping procedure. In other words, given the strong SOC and large $j \approx 3/2$ to $j \approx 1/2$ excitation energies, the initial 36×36 problem can be smoothly mapped onto a 4×4 construction as defined by the effective Hamiltonian (1).

All computations were carried out with the MOLPRO quantum-chemistry software [29]. In the MRCI treatment, single and double excitations from the six Ir (Rh) t_{2g} orbitals and from the $2p$ shells of the bridging O ligand sites were taken into account. The Pipek-Mezey localization module [30] available in MOLPRO was employed for separating the metal $5d$ ($4d$) and O $2p$ valence orbitals into different groups. To derive the magnitude of direct exchange, we additionally performed calculations in which the active space is again defined by ten electrons and six orbitals but intersite t_{2g}-t_{2g} excitations are forbidden by restricting to maximum five the number of electrons per TM site. We refer to these results as rAS (restricted active space, maximum one hole per site).

A. $[Ir_2O_9]$ unit

Effective magnetic couplings for Ir_2O_9 fragments of two face-sharing IrO_6 octahedra are listed in Table I, for an Ir-Ir interatomic distance $d_0 = 2.63$ Å and ligand coordinates that provide Ir-O-Ir angles $\theta_0 = 80^\circ$. These structural parameters, obtained by averaging the bond lengths and bond angles in the experimentally determined lattice configuration of $BaIrO_3$ [17], correspond to slightly elongated octahedra. For cubic (undistorted) octahedra, $\theta_c = 70.52^\circ$. Results at three different levels of approximation are shown: spin-orbit rAS (rAS+SOC), CASSCF (CAS+SOC), and MRCI (CI+SOC) in Table I.

The rAS data account for only direct d-d exchange. For $d_0 = 2.63$ Å and $\theta_0 = 80^\circ$, the rAS $\bar{J}$ is -14.9 meV while the anisotropic $\bar{\Gamma}$ is -0.7 meV when including SOC. The magnitude of the ferromagnetic (FM) rAS $\bar{J}$ is similar to that computed in square-lattice $3d^9$ Cu oxides [31–34] and in the corner-sharing iridate Ba_2IrO_4 [35]. The anisotropic $\bar{\Gamma}$ is also FM at the rAS level and its magnitude is slightly larger as compared with the AFM rAS $\bar{\Gamma}$ of the corner-sharing iridate Ba_2IrO_4 [35]. By CASSCF and MRCI, the singlet Ψ_S becomes the ground state, well below the "triplet" components Ψ_1, Ψ_2, and Ψ_3. This indicates that the isotropic Heisenberg exchange $\bar{J}$ ($\bar{J} > 0$) defines now the largest energy scale. In the CASSCF approximation, only t_{2g}-t_{2g} intersite excitations are accounted for, i.e., t_{2g}^6-t_{2g}^4 configurations. The $\bar{J}$ value extracted by CAS+SOC, 72 meV, is twice as large as compared, e.g., to the CASSCF J's in layered $3d^9$ cuprates [31–34] and in the corner-sharing iridate Ba_2IrO_4 [35]. In the configuration-interaction treatment, which includes TM t_{2g} to e_g and charge-transfer O $2p$ to Ir $5d$ excitations as well, $\bar{J}$ is 123.3 meV, about 70% larger as compared to the CAS+SOC result. By accounting for correlation effects, the symmetric anisotropic coupling $\bar{\Gamma}$ is also significantly enlarged, from -0.7 meV by rAS+SOC to 6.3 meV by spin-orbit MRCI.

In the case of face-sharing ligand octahedra, the TM ions often form dimers, trimers, or chains [17]. This type of low-dimensional packing usually results in sizable distortions of the ligand cages. It is known that the effective spin interactions are strongly dependent on structural details such as bond angles [36–39] and bond lengths [40]. For better insight into the dependence of the NN magnetic couplings on such structural parameters, we performed additional calculations for distorted geometries with all ligands pushed closer to (or farther from) the Ir-Ir axis, which therefore yields larger (or smaller) Ir-O-Ir bond angles while keeping the overall D_{3h} point-group symmetry. The resulting MRCI+SOC data are provided in Table II. The overall trends for the magnetic couplings $\bar{J}$ and $\bar{\Gamma}$ are illustrated graphically in Fig. 2(a). It is seen that the angle dependence for both $\bar{J}$ and $\bar{\Gamma}$ can be rather well reproduced with parabolic curves. The Heisenberg $\bar{J}$ displays a steep increase with larger angle, i.e., from 58 meV at 70.5° to 417 meV at 90°. On the other hand, the anisotropic coupling $\bar{\Gamma}$ shows a rapid decrease, from a remarkably large value of 30 meV at 70.5° to 2 meV at 90°.

We further analyzed the dependence on the Ir-Ir interatomic distance d(Ir-Ir) of the magnetic interactions. In this set of calculations, the distance between the O ligands and the z axis (along the Ir-Ir bond) was fixed to 1.57 Å, while d(Ir-Ir) was either increased or reduced by up to 5% with respect to the reference Ir-Ir separation $d = d_0 = 2.63$ Å. As shown in Fig. 2(b) (see also Appendix B, Table VII), both $\bar{J}$ and $\bar{\Gamma}$ have again pronounced parabolic dependence on d(Ir-Ir). In contrast to the variations as a function of angle displayed in Fig. 2(a), here $\bar{J}$ and $\bar{\Gamma}$ follow the same trend. More

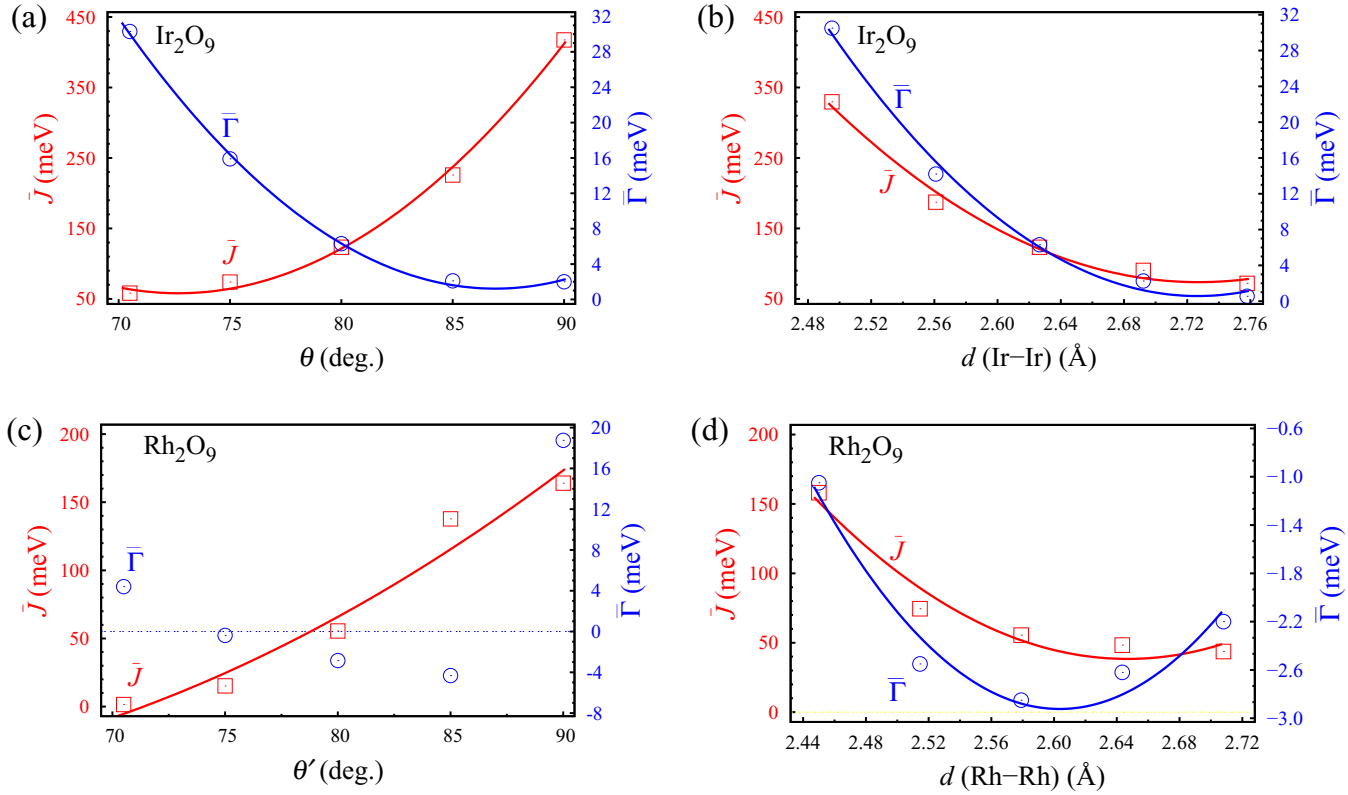

FIG. 2. Dependence on structural details of the NN effective magnetic couplings for Ir_2O_9 and Rh_2O_9 fragments of face-sharing octahedra, spin-orbit MRCI results. [(a) and (c)] Variations as a function of the Ir-O-Ir bond angle θ and Rh-O-Rh bond angle θ' when fixing the Ir-Ir distance to $d_0 = 2.63$ Å and the Rh-Rh distance to $d_0' = 2.58$ Å. Ligands are radially displaced in planes perpendicular to the z axis. Curves were drawn as a guide to the eye; a simple fit is not possible for $\bar{\Gamma}$ in the case of $4d$ magnetic sites. [(b) and (d)] Variations as a function of the TM-TM interatomic distance when keeping unchanged the positions of the ligands. The latter are at distances of $r_0 = 1.57$ Å (Ir_2O_9) and $r_0' = 1.54$ Å (Rh_2O_9) from the z axis.

specifically, both $\bar{J}$ and $\bar{\Gamma}$ rapidly increase with decreasing d(Ir-Ir).

We also performed calculations in which the six O ligands not shared by the Ir ions were displaced as well along the z axis, such that each Ir site remains in the center of the respective octahedron. We found that the differences between the $\bar{J}$ values obtained from these computations and the corresponding $\bar{J}$'s in Fig. 2(a) are rather small, not more than 15%.

The face-sharing linkage and additional distortions applied to the two-octahedra clusters split the t_{2g} levels into a_{1g} and e_g^π components. For all Ir_2O_9 units considered here, we find that the a_{1g} sublevels lie at lower energy and that the t_{2g} hole has e_g^π character without accounting for SOC. The a_{1g} orbitals belonging to NN sites have substantial direct overlap [see Fig. 3(a)], much larger than in the case of e_g^π orbitals [see Fig. 3(b)]. The rather small AFM Heisenberg $\bar{J}$ derived from the calculations without SOC (see caption of Table I) is therefore the result of (relatively) weak direct exchange involving the higher-lying e_g^π states. By accounting for spin-orbit interactions, however, the Heisenberg J is enhanced to impressive values that are up to three times larger than the results obtained without SOC (72 versus 27 meV at the CASSCF level, 123 versus 35 meV by MRCI, see Table I). This strong increase of the Heisenberg J is the consequence of mixing a_{1g} character to the spin-orbit ground-state wave function.

B. [Rh_2O_9] unit

In order to make a informative comparison between $5d$ and $4d$ oxides, we also performed calculations for the effective magnetic couplings on [Rh_2O_9] fragments consisting of two face-sharing RhO_6 octahedra, with a Rh-Rh interatomic distance $d_0' = 2.58$ Å and Rh-O-Rh bond angles $\theta_0' = 80°$. As for the material model of face-sharing $5d^5$ octahedra,

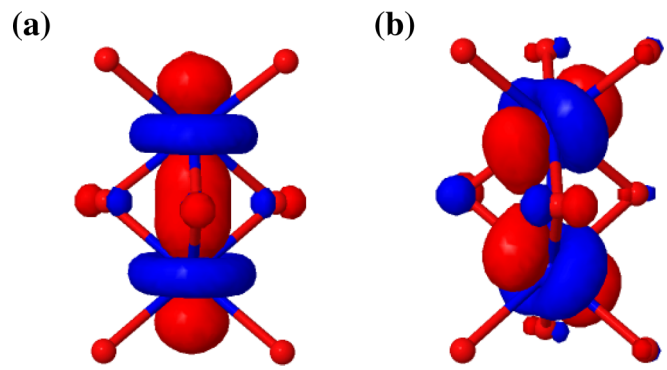

FIG. 3. Natural orbitals of a_{1g} (a) and e_g^π (b) type for a Ir_2O_9 fragment of face-sharing octahedra, as obtained by CASSCF calculations. The former have strong σ-type overlap.

TABLE III. Energy splittings for the lowest four spin-orbit states of two face-sharing NN RhO_6 octahedra and the corresponding effective coupling constants at different levels of approximation, for $d_0' = 2.58$ Å and $\theta_0' = 80°$ (all in meV). The J values without SOC by rAS, CAS, and CI are −0.9, 19.0, and 29.4 meV, respectively.

	rAS+SOC	CAS+SOC	CI+SOC
$\Psi_S = (\|\uparrow\downarrow\rangle - \|\downarrow\uparrow\rangle)/\sqrt{2}$	16.0	0.0	0.0
$\Psi_3 = (\|\uparrow\uparrow\rangle - \|\downarrow\downarrow\rangle)/\sqrt{2}$	0.0	25.4	54.0
$\Psi_1 = (\|\uparrow\downarrow\rangle + \|\downarrow\uparrow\rangle)/\sqrt{2}$	0.0	25.4	54.0
$\Psi_2 = (\|\uparrow\uparrow\rangle + \|\downarrow\downarrow\rangle)/\sqrt{2}$	1.1	26.5	55.5
$\bar{J}, \bar{\Gamma}$	−14.9, −2.3	26.5,−2.2	55.5,−2.8

the structural parameters of the Rh_2O_9 cluster were chosen according to the average bond lengths and bond angles of the $BaRhO_3$ compound. We used in this regard the crystallographic data reported in Ref. [17]. QC results are presented in Table III. Interestingly, the $\bar{J}$ value obtained by spin-orbit rAS is the same as for the Ir_2O_9 cluster (Table I). However, the $\bar{J}$'s obtained by CAS+SOC and CI+SOC are significantly smaller as compared with those in Table I. Still, $\bar{J}$ remains much larger than the magnetic couplings in the edge-sharing $4d^5$ compounds Li_2RhO_3 and α-$RuCl_3$ [37,38].

Energy splittings within the group of the four low-lying d^5-d^5 states and the resulting effective coupling constants for different Rh-O-Rh angles are listed in Table IV. Furthermore, the dependence of $\bar{J}$ and $\bar{\Gamma}$ on the Rh-O-Rh bond angles and on the Rh-Rh interatomic distances are illustrated in Figs. 2(c) and 2(d), respectively (for more details see Appendix B, Tables VIII and IX). As indicated in Fig. 2(c), $\bar{J}$ displays nearly linear behavior with variable angle, increasing from 1.5 meV at 70.5° to 164 meV at 90°. $\bar{\Gamma}$ changes sign from AFM to FM coupling close to 75°, with a minimum of −6 meV at85°, and then changes back to AFM values for larger angles. On the other hand, with variable d(Rh-Rh) [Fig. 2(d)], $\bar{\Gamma}$ is always FM, with a minimum of −2.8 meV at 2.56 Å, and $\bar{J}$ features a similar trend as for Ir sites in Fig. 2(b).

IV. DISCUSSION

We analyze in more detail in this section the relative values of the different contributions to intersite exchange, i.e., direct t_{2g}-t_{2g} exchange, t_{2g}-t_{2g} electron/hole hopping, and indirect hopping via the bridging oxygens. In first place, it is clear

TABLE IV. Energy splittings and the corresponding effective coupling constants for variable Rh-O-Rh angle, MRCI+SOC results (meV). The NN Rh-Rh distance is 2.58 Å. The Rh-O-Rh angle θ' is listed for each geometry; distances between Rh and the bridging O's, d(Rh-O), are provided within brackets.

	70.5°(2.23Å)	75°(2.12Å)	80°(2.04Å)	85°(1.91Å)	90°(1.82Å)
Ψ_S	0.0	0.0	0.0	0.0	0.0
Ψ_3	3.7	15.0	54.0	135.7	173.4
Ψ_1	3.7	15.0	54.0	135.7	173.4
Ψ_2	1.5	15.2	55.5	137.8	164.0
$\bar{J}, \bar{\Gamma}$	1.5, 4.4	15.2,−0.4	55.5,−2.8	137.8,−4.3	164.0, 18.8

TABLE V. Angle dependence of the trigonal CF splitting Δ_t (eV) obtained from MRCI calculations for Ir_2O_9 and Rh_2O_9 fragments of face-sharing octahedra. The a_{1g} level is for all angles the lowest in energy.

θ/θ'	Δ_t^{Ir}	Δ_t^{Rh}
70.5	−0.86	−0.69
75	−0.89	−0.67
80	−0.71	−0.53
85	−0.43	−0.29
90	−0.20	−0.10

that a systematically small portion of FM potential exchange to the overall $\bar{J}$ is here of secondary importance. The contribution coming from direct hopping can be straightforwardly estimated from the CASSCF J since only intersite $M(t_{2g})$–$M(t_{2g})$ excitation processes (t_{2g}^6-t_{2g}^4 polar configurations) are taken into account at the CASSCF level. In the CI treatment, superexchange paths including the bridging-ligand $2p$ and TM e_g orbitals are also added on top of direct hopping, providing a more comprising description of intersite exchange mechanisms.

In the case of $BaIrO_3$, for instance, when the Ir-O-Ir bond angle is 80°, the exchange calculated at the CASSCF level (without SOC), $J = 27.4$ meV, is already 77% of the CI result, 35.4 meV (see Table I). While this fraction is significantly reduced if the Ir-O-Ir bond angle is modified towards 90° (see Table VI), indicating that the d-p-d superexchange contribution starts to rise as a result of shorter Ir-O bonds, the data computed for 80° bond angles show that, given the large direct-hopping integrals, the direct AFM d-d superexchange may surpass the d-p-d superexchange. The two mechanisms should be considered in any case on equal footing for high-quality estimates. In the context of recent discussions on the role of the various types of intersite exchange [41,42], our QC data provide a more quantitative picture on the different contributions.

Given the facet-sharing geometry, the direct d-d electron/hole hopping between a_{1g} orbitals is considerable. This hopping interferes with the indirect hopping via the bridging-oxygen O_3 group, providing a total transfer integral t. Since the exchange coupling J is mainly controlled by the square of t ($J \sim t^2/U$, where U is the on-site Coulomb repulsion), a large $\bar{J}$ value of up to ≈ 400 meV (see Tables VI and VII) is not surprising. Both the direct ($\sim t^{dd}$) and indirect ($\sim t^{dpd}$) transfer processes can occur trough the e_g^π and a_{1g} channels independently. As discussed in Appendix A, the total transfer integral t can be then decomposed as $t = w_e t_e + w_a t_a$, where $t_{e,a} = t_{e,a}^{dd} + t_{e,a}^{dpd}$. The corresponding channel weights, w_e and w_a, are controlled by the ratio Δ_t/λ, with λ being the spin-orbit coupling, 0.47 eV for Ir and 0.15 eV for Rh [43]; the dependence of the trigonal splitting Δ_t on bond angles is illustrated in Table V. The different terms entering the total transfer integral t are expected to behave differently when varying the geometry of the M-O_3-M structure. The large direct overlap between two NN a_{1g} orbitals suggests that the direct hopping t_a^{dd} contributes significantly to t_a, as evidenced in Fig. 3. In contrast, the e_g^π orbitals are tilted with

TABLE VI. Energy splittings for the lowest four spin-orbit states of two face-sharing NN IrO_6 octahedra and the corresponding effective coupling constants obtained from rAS+SOC, CAS+SOC, and MRCI+SOC calculations. For each geometry, the Ir-Ir distance was fixed to 2.63Å. For $\theta = 90^\circ$, for instance, the J values without SOC by rAS, CAS, and CI are 0.04, 64.7, and 116.4 meV, respectively. Distances between the Ir sites and the bridging O's, d(Ir-O), are provided within brackets. The data are presented as complementary to those in Table II (all values in meV).

θ, d(Ir-O)	rAS+SOC	CASSCF+SOC	MRCI+SOC
70.5° (2.27 Å):			
Ψ_S	9.9	0.0	0.0
Ψ_2	0.0	24.8	58.2
Ψ_1	0.5	34.9	73.4
Ψ_3	0.5	34.9	73.4
$\bar{J}$, $\bar{\Gamma}$	−9.9, 1.1	24.8, 20.3	58.2, 30.3
75° (2.16 Å):			
Ψ_S	12.8	0.0	0.0
Ψ_2	0.0	36.3	73.9
Ψ_1	0.0	41.6	81.8
Ψ_3	0.0	41.6	81.8
$\bar{J}$, $\bar{\Gamma}$	−12.8, 0.0	36.3, 10.5	73.9, 15.9
80° (2.04 Å):			
Ψ_S	15.2	0.0	0.0
Ψ_2	0.4	72.0	123.3
Ψ_1	0.0	74.0	126.5
Ψ_3	0.0	74.0	126.5
$\bar{J}$, $\bar{\Gamma}$	−14.9, −0.7	72.0, 4.1	123.3, 6.3
85° (1.94 Å):			
Ψ_S	16.2	0.0	0.0
Ψ_2	0.3	149.4	225.8
Ψ_1	0.0	150.1	226.9
Ψ_3	0.0	150.1	226.9
$\bar{J}$, $\bar{\Gamma}$	−15.9, −0.6	149.4, 1.3	225.8, 2.1
90° (1.86 Å):			
Ψ_S	17.0	0.0	0.0
Ψ_2	0.0	293.6	417.5
Ψ_1	0.3	294.2	418.5
Ψ_3	0.3	294.2	418.5
$\bar{J}$, $\bar{\Gamma}$	−17.0, 0.7	293.6, 1.2	417.5, 2.0

TABLE VII. Energy splittings for the lowest four spin-orbit states of two face-sharing NN IrO_6 octahedra and the corresponding effective coupling constants obtained from rAS+SOC, CAS+SOC, and MRCI+SOC calculations. The relative distances from the O ligands to the z axis were fixed to 1.57 Å. The data are presented as complementary to those in Fig. 2(b) (all values in meV).

d(Ir-Ir)	rAS+SOC	CASSCF+SOC	MRCI+SOC
2.50 Å:			
Ψ_S	22.0	0.0	0.0
Ψ_2	0.5	188.6	329.7
Ψ_1	0.0	198.1	345.0
Ψ_3	0.0	198.1	345.0
$\bar{J}$, $\bar{\Gamma}$	−21.5 − 0.93	188.6, 18.9	329.7, 30.5
2.56 Å:			
Ψ_S	18.3	0.0	0.0
Ψ_2	0.4	106.7	187.2
Ψ_1	0.0	111.2	194.3
Ψ_3	0.0	111.2	194.3
$\bar{J}$, $\bar{\Gamma}$	−17.9, −0.8	106.7, 8.9	187.2, 14.2
2.63 Å:			
Ψ_S	15.2	0.0	0.0
Ψ_2	0.4	72.0	123.3
Ψ_1	0.0	74.0	126.5
Ψ_3	0.0	74.0	126.5
$\bar{J}$, $\bar{\Gamma}$	−14.9, −0.7	72.0, 4.1	123.3, 6.3
2.69 Å:			
Ψ_S	12.6	0.0	0.0
Ψ_2	0.3	54.7	90.5
Ψ_1	0.0	55.5	91.7
Ψ_3	0.0	55.5	91.7
$\bar{J}$, $\bar{\Gamma}$	−12.4, −0.54	54.7, 1.7	90.5, 2.2
2.76 Å:			
Ψ_S	10.4	0.0	0.0
Ψ_2	0.2	44.5	72.1
Ψ_1	0.0	44.8	72.4
Ψ_3	0.0	44.8	72.4
$\bar{J}$, $\bar{\Gamma}$	−10.3, −0.4	44.5, 0.6	72.1, 0.5

respect to the z axis, thus giving rise to weaker direct overlap and more significant d-p-d couplings [see Fig. 3(b)], i.e., a more important role of t_e^{dpd} in t_e. It is the interplay between these processes, d-d and d-p-d superexchange, that is mainly responsible for the strong variations as a function of bond angles and bond lengths.

From a wider perspective, it is clear that the equilibrium geometrical configuration and the associated J value depend on interactions and degrees of freedom that also involve the extended crystalline surroundings. An interesting aspect to be considered is inter-site couplings within the entire M_3O_{12} block of three face-sharing octahedra along the c axis [see Fig. 1(a)]. One question concerns the possibility of cooperative M-M dimerization as driving force for the charge density wave observed in $BaIrO_3$ [10]. Two-site bond formation on three-center units with a spin 1/2 at each magnetic site and long-range ordering of these "dimers" has been earlier proposed in the quasi-1D system NaV_2O_5 [44,45].

To summarize, we employ quantum chemistry methods to provide valuable insights on the effective magnetic interactions in 5d and 4d oxides with face-sharing oxygen octahedra, $BaIrO_3$ and $BaRhO_3$. The same methodology has previously been used to derive magnetic coupling constants in good agreement with experimental estimates in the perovskite iridate $CaIrO_3$ [25,46], in square-lattice Ba_2IrO_4 [35] and Sr_2IrO_4 [8], and in pyrochlore iridates [39]. The large AFM Heisenberg interactions computed here for face-sharing octahedra are remarkable since they exceed the values computed so far for corner-sharing [20,25,33,35] and edge-sharing systems [36]. One peculiar exception with regard to edge-sharing $4d^5$ NN ligand cages is $RuCl_3$ under high pressure [47], where a strong stabilization of the singlet state is also found for certain Ru-Ru bonds. The present findings on face-sharing octahedra as encountered in $BaIrO_3$ and $BaRhO_3$ and recent results on $RuCl_3$ [47] only provide additional motivation for even more detailed electronic-structure calculations on both

edge- and face-sharing compounds, with main focus on the subtle interplay among strong spin-orbit interactions, direct d-d orbital overlap and bonding, and couplings to the lattice degrees of freedom.

ACKNOWLEDGMENTS

Calculations were performed at the High Performance Computing Center (ZIH) of the Technical University Dresden (TUD). We thank U. Nitzsche for technical assistance. We acknowledge financial support from the German Science Foundation (Deutsche Forschungsgemeinschaft, DFG — HO-4427/2 and SFB-1143) and thank D. I. Khomskii, V. M. Katukuri, N. A. Bogdanov, and S.-L. Drechsler for instructive discussions.

APPENDIX A: EFFECTIVE SPIN MODEL

To put in perspective the general trends obtained in the QC calculations for the isotropic exchange coupling J, an effective two-site model is analyzed here. Two different mechanisms are considered: (a) direct $t_{2g}-t_{2g}$ hopping $\sim t^{dd}$ and (b) indirect processes via the bridging oxygens, $\sim t^{dpd}$. The three bridging oxygens within the median xy mirror plane are denoted as O_n, with $n \in \{1,2,3\}$. For each metal ion at sites $l = A, B$, the trigonal CF term $\mathcal{H}_{\mathrm{CF},t}$ splits the t_{2g} orbital states into a two- and an one-dimensional subspace with basis states $|e_{1l}\rangle$, $|e_{2l}\rangle$ and $|a_l\rangle$, respectively [48]. In what follows, these hole states are denoted as $|\phi_{\mu l}\rangle$, with $\mu = 1,2$ for $|e_{1,2}\rangle$, $\mu = 3$ for $|a\rangle$, and the creation (annihilation) operator $\phi^{\dagger}_{\mu l,\sigma}$ ($\phi_{\mu l,\sigma}$), where the spin variable $\sigma = \pm 1/2$ is added. Restricted to this low-energy orbital space, a single hole is described by the effective orbital angular momentum operator $L = 1$ [48] in the spin-orbit term $\mathcal{H}_{\mathrm{SO}} = \lambda \sum_l \mathbf{L}_l \mathbf{S}_l$; here, $\mathbf{S}$ is the spin-1/2 operator and $\lambda > 0$. Altogether, relevant intra-atomic interactions are collected in the effective Hamiltonian $\mathcal{H}_{\mathrm{at}} = \mathcal{H}_{\mathrm{CF},t} + \mathcal{H}_{\mathrm{SO}} + \mathcal{H}_U$, where

$$\mathcal{H}_{\mathrm{CF},t} + \mathcal{H}_{\mathrm{SO}} = \frac{\Delta_t}{3} \sum_l \sum_{\mu,\sigma} (\delta_{\mu 1} + \delta_{\mu 2} - 2\delta_{\mu 3}) \phi^{\dagger}_{\mu l,\sigma} \phi_{\mu l,\sigma} + \lambda \sum_{\mu\mu'} \sum_{\sigma\sigma'} [\mathbf{L}_l]_{\mu\mu'} \cdot [\mathbf{S}_l]_{\sigma\sigma'} \phi^{\dagger}_{\mu l,\sigma} \phi_{\mu' l,\sigma'}. \tag{A1}$$

Here, $[\mathbf{L}_l]_{\mu\mu'} = \langle \phi_{\mu l} | \mathbf{L}_l | \phi_{\mu' l} \rangle$ while Δ_t is the trigonal CF splitting between $|e_{1,2}\rangle$ and $|a\rangle$ "local" states. As stated in the main text, without SOC the calculated hole ground state of Ir^{4+}/Rh^{4+} ions is of e-orbital character, which means $\Delta_t < 0$. The term $\mathcal{H}_U$ includes the leading on-site Coulomb interaction

$$\mathcal{H}_U = \frac{U}{2} \sum_l \sum_{\mu\mu'} \sum_{\sigma\sigma'} n_{\mu l,\sigma} n_{\mu' l,\sigma'}, \tag{A2}$$

where $n_{\mu l,\sigma} = \phi^{\dagger}_{\mu l,\sigma} \phi_{\mu l,\sigma}$. The approximation of assuming the Coulomb U in the above expression to be independent of the orbital indices μ and μ' simplifies the calculation of the isotropic exchange J but excludes obtaining an estimate for the weaker anisotropic exchange Γ.

Within the one-hole sector and in the cubic limit $\Delta_t \to 0$, $\mathcal{H}_{\mathrm{at}}$ is reduced to $\mathcal{H}_{\mathrm{SO}}$. As well known [48], the "original" six $L = 1$ atomic states $|L_z = 0, \pm 1; \sigma = \pm 1/2\rangle$ are split by $\mathcal{H}_{\mathrm{SO}}$ into the Kramers doublet $|j = 1/2; m = \pm 1/2\rangle$ and the quartet $|j = 3/2; m = \pm 1/2, \pm 3/2\rangle$, whose eigenvalues are $-\lambda$ and $\lambda/2$, respectively; here, the site index l is omitted for brevity. When lowering the CF symmetry to trigonal, i.e., $\Delta_t \neq 0$, states with the same $m(= \pm 1/2)$, $|j = 1/2; m\rangle$ and $|j = 3/2; m\rangle$, are admixed. By solving the corresponding 2×2 problem, the resulting doublet wave functions are $|\psi_1(m = \pm 1/2)\rangle = c_1 |1/2; m\rangle \pm c_2 |3/2; m\rangle$ and $|\psi_2(m = \pm 1/2)\rangle = \mp c_2 |1/2; m\rangle + c_1 |3/2; m\rangle$, where $c_{1,2} = [1/2(1 \pm A/\sqrt{A^2 + B^2})]^{1/2}$ and $A = 3 - \delta$, $B = 2\sqrt{2}\delta$, $\delta = 2\Delta_t/3\lambda$. The corresponding eigenvalues are $E_{1,2} = (-\lambda/4)[1 + 3\delta \pm 3\sqrt{1 - 2\delta/3 + \delta^2}]$ and, since $\lambda > 0$, $E_1 < E_2$. The energy of the remaining doublet, $|\psi_3(m)\rangle = |j = 3/2; m = \pm 3/2\rangle$, is $E_3 = \lambda/2$.

In general, the initial and new basis states are related by an unitary transformation with the rotation matrix $U_{km,\mu\sigma}$ (here, the site index l is restored):

$$|\phi_{\mu l}; \sigma\rangle = \sum_{k,m} |\psi_{kl}(m)\rangle U_{km,\mu\sigma}. \tag{A3}$$

Close inspection of the above expressions for the E_k energy levels ($k = 1, 2, 3$) shows that the ground-state doublet ($k = 1$) is well separated from the excited ones ($k = 2, 3$) for any Δ_t; the low-energy magnetic properties of the system are therefore described by pseudospin-1/2 states $|\psi_{1l}(m)\rangle$. Projection on the low-energy subspace consists in retaining in Eq.(A3) the term $k = 1$ only, which reads with the replacement $m \to s$ as

$$\begin{aligned} |a_l; \sigma = \pm 1/2\rangle &\to \mp \cos\gamma \; |\psi_{1l}(s = \pm 1/2)\rangle, \\ |e_{1l}; \sigma = \pm 1/2\rangle &\to \frac{1}{\sqrt{2}} \sin\gamma \; |\psi_{1l}(s = \pm 1/2)\rangle, \\ |e_{2l}; \sigma = \pm 1/2\rangle &\to \pm \frac{i}{\sqrt{2}} \sin\gamma \; |\psi_{1l}(s = \mp 1/2)\rangle, \end{aligned} \tag{A4}$$

where $\cos\gamma = (c_1 - \sqrt{2}c_2)/\sqrt{3}$ and $\sin\gamma = (\sqrt{2}c_1 + c_2)/\sqrt{3}$. In the following, the creation (annihilation) of state $|\psi_{1l}(s)\rangle$ is associated with the operator $\psi^{\dagger}_{1l,s}$ ($\psi_{1l,s}$). Projected onto the pseudospin-1/2 subspace, the Coulomb interaction $\mathcal{H}_U$ takes the Hubbard-like form $\mathcal{H}_U = U \sum_l n_{1l,\uparrow} n_{1l,\downarrow}$. Actually, the unitary transformation (A3) yields $\sum_{\mu,\sigma} n_{\mu l,\sigma} = \sum_{k,m} n_{kl,m}$, where only the term $k = 1$ is kept.

In case of face-sharing octahedra, the relatively short M_A-M_B distance dictates inclusion of the direct t_{2g}-t_{2g} hopping term

$$\mathcal{H}^{dd}_{\mathrm{hop}} = \sum_{\mu,\sigma} t^{dd}_{\mu\mu} (\phi^{\dagger}_{\mu A,\sigma} \phi_{\mu B,\sigma} + \mathrm{H.c.}). \tag{A5}$$

The precise structure of $\mathcal{H}^{dd}_{\mathrm{hop}}$ is determined by symmetry arguments that require that (a) the off-diagonal hopping is zero, i.e., $t^{dd}_{\mu\mu'} = 0$ if $\mu \neq \mu'$ and (b) there are two independent hopping integrals, namely, $t^{dd}_{11} = t^{dd}_{22} \equiv t^{dd}_e$ and $t^{dd}_{33} \equiv t^{dd}_a$. Projection onto the low-energy subspace then leads to

$$\mathcal{H}^{dd}_{\mathrm{hop}} \simeq t^{dd} \sum_s (\psi^{\dagger}_{1A,s} \psi_{1B,s} + \mathrm{H.c.}), \tag{A6}$$

TABLE VIII. Energy splittings for the lowest four spin-orbit states of two face-sharing NN RhO_6 octahedra and the corresponding effective coupling constants obtained from rAS+SOC, CAS+SOC, and MRCI+SOC calculations. For each geometry, the Rh-Rh distance was fixed to 2.58 Å. Distances between the Rh sites and the bridging O's, d(Rh-O), are provided within brackets. The data are presented as complementary to those in Table IV (all values in meV).

θ, d(Rh-O)	rAS+SOC	CASSCF+SOC	MRCI+SOC
70.5° (2.23 Å):			
Ψ_S	10.4	6.5	0.0
Ψ_3	0.0	1.0	3.7
Ψ_1	0.0	1.0	3.7
Ψ_2	0.6	0.0	1.5
$\bar{J}, \bar{\Gamma}$	−9.9 − 1.1	−6.5, 2.0	1.5, 4.4
75° (2.12 Å):			
Ψ_S	13.3	0.0	0.0
Ψ_3	0.0	0.1	15.0
Ψ_1	0.0	0.1	15.0
Ψ_2	0.8	0.4	15.2
$\bar{J}, \bar{\Gamma}$	−12.5, −1.7	0.4, −0.6	15.2, −0.4
80° (2.06 Å):			
Ψ_S	16.0	0.0	0.0
Ψ_3	0.0	25.4	54.0
Ψ_1	0.0	25.4	54.0
Ψ_2	1.1	26.5	55.5
$\bar{J}, \bar{\Gamma}$	−14.9, −2.3	26.5, −2.2	55.5, −2.8
85° (1.91 Å):			
Ψ_S	17.7	0.0	0.0
Ψ_3	0.0	82.4	135.7
Ψ_1	0.0	82.4	135.7
Ψ_2	1.3	84.0	137.8
$\bar{J}, \bar{\Gamma}$	−16.4, −2.6	84.0, −3.2	137.8, −4.3
90° (1.82 Å):			
Ψ_S	16.5	0.0	0.0
Ψ_3	0.0	165.4	173.4
Ψ_1	0.0	165.4	173.4
Ψ_2	0.9	190.5	164.0
$\bar{J}, \bar{\Gamma}$	−15.6, −1.8	190.5, −50.2	164.0, 18.8

TABLE IX. Energy splittings for the lowest four spin-orbit states of two face-sharing NN RhO_6 octahedra and the corresponding effective coupling constants obtained from rAS+SOC, CAS+SOC, and MRCI+SOC calculations. The relative distances from the O ligands to the z axis are fixed to 1.54 Å. The data are presented as complementary to those in Fig. 2(b) (all values in meV).

d(Rh-Rh)	rAS+SOC	CASSCF+SOC	MRCI+SOC
2.45 Å:			
Ψ_S	22.0	0.0	0.0
Ψ_3	0.0	49.5	157.6
Ψ_1	0.0	49.5	157.6
Ψ_2	1.6	50.0	158.1
$\bar{J}, \bar{\Gamma}$	−20.4 − 3.2	50.0, −1.1	158.1, −1.1
2.51 Å:			
Ψ_S	18.8	0.0	0.0
Ψ_3	0.0	30.1	73.2
Ψ_1	0.0	30.1	73.2
Ψ_2	1.4	31.1	74.5
$\bar{J}, \bar{\Gamma}$	−17.5, −2.7	31.1, −2.1	74.5, −2.5
2.58 Å:			
Ψ_S	16.0	0.0	0.0
Ψ_3	0.0	25.4	54.0
Ψ_1	0.0	25.4	54.0
Ψ_2	1.1	26.5	55.5
$\bar{J}, \bar{\Gamma}$	−14.9, −2.3	26.5, −2.2	55.5, −2.8
2.64 Å:			
Ψ_S	13.6	0.0	0.0
Ψ_3	0.0	23.8	47.0
Ψ_1	0.0	23.8	47.0
Ψ_2	1.0	24.7	48.3
$\bar{J}, \bar{\Gamma}$	−12.6, −1.9	24.7, −2.0	48.3, −2.6
2.71 Å:			
Ψ_S	11.5	0.0	0.0
Ψ_3	0.0	22.6	42.6
Ψ_1	0.0	22.6	42.6
Ψ_2	0.8	23.5	43.7
$\bar{J}, \bar{\Gamma}$	−10.7, −1.6	23.5, −1.7	43.7, −2.2

where $t^{dd} = t_e^{dd} \sin^2\gamma + t_a^{dd} \cos^2\gamma$. Obviously, variation of the M_A-M_B distance d_{MM} gives rise to strong variation of the hopping integral t^{dd}. The a-channel contribution $\sim t_a^{dd}$ is expected to be most sensitive to varying d_{MM}. For instance, according to [49] $t_a^{dd} \sim d_{MM}^{-5}$.

The treatment of indirect hopping processes via the bridging oxygens is a challenging problem. The M-O_3-M unit should be viewed as a complex molecular-like structure, where superexchange couplings must be analyzed in terms of symmetry-adapted molecular orbitals of the O_3 bridging group. A detailed analysis shows that in the low-energy subspace the indirect hopping term $\mathcal{H}_{\rm hop}^{dpd}$ has the same structure as $\mathcal{H}_{\rm hop}^{dd}$, Eq.(A6), with the replacement $t^{dd} \to t^{dpd} = t_e^{dpd} \sin^2\gamma + t_a^{dpd} \cos^2\gamma$. The hopping integrals $t_{e,a}^{dpd}$ due to second-order processes that occur through intermediate ligand-hole states in the e and a channels, respectively, can be expressed in factorized form as $t_{e,a}^{dpd} \approx [(t^{dp})^2/\Delta_{\rm CT}]F_{e,a}(\theta)$. Here, t^{dp} and $\Delta_{\rm CT}$ define the characteristic p-d hopping and charge-transfer energy scales. While the factor $F_{e,a}(\theta)$ is strongly dependent on the angle θ, the parameter t^{dp} is most sensitive to the metal-oxygen distance d_{MO}. According to [49], $t^{dp} \sim d_{MO}^{-7/2}$. Transitions of first-order ($\sim t_{a,e}^{dd}$) and second-order types ($\sim t_{a,e}^{dpd}$) contribute in each sector independently to give the total transfer integral $t = t_e \sin^2\gamma + t_a \cos^2\gamma$, where $t_{e,a} = t_{e,a}^{dd} + t_{e,a}^{dpd}$. The resultant hopping Hamiltonian $\mathcal{H}_{\rm hop}$ takes the same form as in Eq. (A6), but with the replacement $t^{dd} \to t$. The weight factors of the e and a channels are $w_e = \sin^2\gamma$ and $w_a = \cos^2\gamma$, respectively. As discussed above, these factors are controlled by the ratio Δ_t/λ.

It is seen that the generic Hamiltonian $\mathcal{H} = \mathcal{H}_{at} + \mathcal{H}_{\rm hop}$ derived above takes the form of an effective "single-orbital" Hubbard model operating in the pseudospin-1/2 subspace of NN metal ions. It can be treated perturbatively in the strong correlation regime $t/U \ll 1$, meaning that excited polar states with two holes on the same metal ion are well separated from the low-energy magnetic excitations. In this regime, one immediately obtains as second-order estimate for the isotropic exchange $J = 4t^2/U$.

APPENDIX B: INTERSITE MAGNETIC COUPLINGS

All computations were performed with the MOLPRO quantum chemistry package [29]. Energy-consistent relativistic pseudopotentials were used for the Ir [50] and Rh [51] ions. For the Ir/Rh sites, the valence orbitals were described by basis sets of tripe-zeta quality supplemented with two f polarization functions [50,51]. For the ligand O's bridging the two magnetically active Ir (Rh) ions, quintuple-zeta valence basis sets and four d polarization functions were applied [52]. The other O's were modeled by triple-zeta valence basis sets [52]. The five Ba ions were modeled by Ba^{2+} "total-ion" pseudopotentials (TIP's) supplemented with a single s function [53]. We used interatomic distances as derived by E. Stitzer *et al.* [17].

The mapping of the *ab initio* quantum chemistry data onto the effective spin model defined by (1) implies the lowest four spin-orbit states associated with the different possible couplings of two NN pseudospins 1/2. In order to safely identify the singlet and triplet components [8], we also consider the Zeeman coupling

$$\hat{\mathcal{H}}^Z = \sum_{l=A,B} \mu_B(\mathbf{L}_l + g_e\mathbf{S}_l)\cdot\mathbf{H}, \tag{B1}$$

where $\mathbf{L}_l$ and $\mathbf{S}_l$ are angular-momentum and spin operators at a given Ir/Rh site, while g_e and μ_B stand for the free-electron Landé factor and Bohr magneton, respectively. Each of the resulting matrix element computed at the quantum chemistry level is assimilated to the corresponding matrix element of the effective spin Hamiltonian. This one-to-one correspondence between *ab initio* and effective-model matrix elements enables a clear assignment of each magnetically active spin-orbit CASSCF/MRCI state and determination of all couplings constants [8]. Effective coupling constants at the rAS+SOC, CAS+SOC, and CI+SOC levels are listed in Tables VI, VII, VIII, and IX, complementary to tables and figures in the main text.

[1] B. J. Kim, H. Jin, S. J. Moon, J.-Y. Kim, B.-G. Park, C. S. Leem, J. Yu, T. W. Noh, C. Kim, S.-J. Oh, J.-H. Park, V. Durairaj, G. Cao, and E. Rotenberg, Novel $j_{\rm eff} = 1/2$ Mott State Induced by Relativistic Spin-Orbit Coupling in Sr_2IrO_4, Phys. Rev. Lett. **101**, 076402 (2008).

[2] B. J. Kim, H. Ohsumi, T. Komesu, S. Sakai, T. Morita, H. Takagi, and T. Arima, Phase-sensitive observation of a spin-orbital Mott state in Sr_2IrO_4, Science **323**, 1329 (2009).

[3] G. Jackeli and G. Khaliullin, Mott Insulators in the Strong Spin-Orbit Coupling Limit: From Heisenberg to a Quantum Compass and Kitaev Models, Phys. Rev. Lett. **102**, 017205 (2009).

[4] A. Kitaev, Anyons in an exactly solved model and beyond, Ann. Phys. **321**, 2 (2006).

[5] Z. Nussinov and J. van den Brink, Compass models: Theory and physical motivations, Rev. Mod. Phys. **87**, 1 (2015).

[6] Y. Yamaji, Y. Nomura, M. Kurita, R. Arita, and M. Imada, First-Principles Study of the Honeycomb-Lattice Iridates Na_2IrO_3 in the Presence of Strong Spin-Orbit Interaction and Electron Correlations, Phys. Rev. Lett. **113**, 107201 (2014).

[7] V. M. Katukuri, S. Nishimoto, V. Yushankhai, A. Stoyanova, H. Kandpal, S. Choi, R. Coldea, I. Rousochatzakis, L. Hozoi, and J. van den Brink, Kitaev interactions between $J = 1/2$ moments in honeycomb Na_2IrO_3 are large and ferromagnetic: Insights from *ab initio* quantum chemistry calculations, New J. Phys. **16**, 013056 (2014).

[8] N. A. Bogdanov, V. M. Katukuri, J. Romhányi, V. Yushankhai, V. Kataev, B. Büchner, J. van den Brink, and L. Hozoi, Orbital reconstruction in nonpolar tetravalent transition-metal oxide layers, Nat. Commun. **6**, 7306 (2015).

[9] R. Lindsay, W. Strange, B.L. Chamberland, and R.O. Moyer, Weak ferromagnetism in $BaIrO_3$, Solid State Commun. **86**, 759 (1993).

[10] G. Cao, J. E. Crow, R. P. Guertin, P. F. Henning, C. C. Homes, M. Strongin, D. N. Basov, and E. Lochner, Charge density wave formation accompanying ferromagnetic ordering in quasi-one-dimensional $BaIrO_3$, Solid State Commun. **113**, 657 (2000).

[11] M. L. Brooks, S. J. Blundell, T. Lancaster, W. Hayes, F. L. Pratt, P. P. C. Frampton, and P. D. Battle, Unconventional magnetic properties of the weakly ferromagnetic metal $BaIrO_3$, Phys. Rev. B **71**, 220411 (2005).

[12] T. Nakano and I. Terasaki, Giant nonlinear conduction and thyristor-like negative differential resistance in $BaIrO_3$ single crystals, Phys. Rev. B **73**, 195106 (2006).

[13] J.-G. Cheng, J.-S. Zhou, J. A. Alonso, J. B. Goodenough, Y. Sui, K. Matsubayashi, and Y. Uwatoko, Transition from a weak ferromagnetic insulator to an exchange-enhanced paramagnetic metal in the $BaIrO_3$ polytypes, Phys. Rev. B **80**, 104430 (2009).

[14] M. A. Laguna-Marco, D. Haskel, N. Souza-Neto, J. C. Lang, V. V. Krishnamurthy, S. Chikara, G. Cao, and M. van Veenendaal, Orbital Magnetism and Spin-Orbit Effects in the Electronic Structure of $BaIrO_3$, Phys. Rev. Lett. **105**, 216407 (2010).

[15] T. Dey, M. Majumder, J. C. Orain, A. Senyshyn, M. Prinz-Zwick, S. Bachus, Y. Tokiwa, F. Bert, P. Khuntia, N. Büttgen, A. A. Tsirlin, and P. Gegenwart, Persistent low-temperature spin dynamics in the mixed-valence iridate $Ba_3InIr_2O_9$, Phys. Rev. B **96**, 174411 (2017).

[16] W. Miiller, M. Avdeev, Q. Zhou, B. J. Kennedy, N. Sharma, R. Kutteh, G.J. Kearley, S. Schmid, K. S. Knight, P. E. R. Blanchard, and C. D. Ling, Giant magnetoelastic effect at the opening of a spin-gap in $Ba_3BiIr_2O_9$, J. Am. Chem. Soc. **134**, 3265 (2012).

[17] K. E. Stitzer, A. El Abed, J. Darriet, and H.-C. zur Loye, Crystal growth and structure determination of barium rhodates: Stepping stones toward 2H-$BaRhO_3$, J. Am. Chem. Soc. **126**, 856 (2004).

[18] J. Sugiyama, H. Nozaki, Y. Ikedo, K. Mukai, D. Andreica, A. Amato, J. H. Brewer, E. J. Ansaldo, G. D. Morris, T. Takami, and H. Ikuta, Evidence of Two Dimensionality in Quasi-One-Dimensional Cobalt Oxides, Phys. Rev. Lett. **96**, 197206 (2006).

[19] H. Suzuura, H. Yasuhara, A. Furusaki, N. Nagaosa, and Y. Tokura, Singularities in Optical Spectra of Quantum Spin Chains, Phys. Rev. Lett. **76**, 2579 (1996).

[20] N. Motoyama, H. Eisaki, and S. Uchida, Magnetic Susceptibility of Ideal Spin 1/2 Heisenberg Antiferromagnetic Chain

Systems, Sr_2CuO_3 and $SrCuO_2$, Phys. Rev. Lett. **76**, 3212 (1996).

[21] G. Cao, X. N. Lin, S. Chikara, V. Durairaj, and E. Elhami, High-temperature weak ferromagnetism on the verge of a metallic state: Impact of dilute Sr doping on $BaIrO_3$, Phys. Rev. B **69**, 174418 (2004).

[22] O. B. Korneta, S. Chikara, S. Parkin, L. E. DeLong, P. Schlottmann, and G. Cao, Pressure-induced insulating state in $Ba_{1-x}R_xIrO_3$ (R = Gd, Eu) single crystals, Phys. Rev. B **81**, 045101 (2010).

[23] M. A. Laguna-Marco, G. Fabbris, N. M. Souza-Neto, S. Chikara, J. S. Schilling, G. Cao, and D. Haskel, Different response of transport and magnetic properties of $BaIrO_3$ to chemical and physical pressure, Phys. Rev. B **90**, 014419 (2014).

[24] S. J. Yuan, K. Butrouna, J. Terzic, H. Zheng, S. Aswartham, L. E. DeLong, F. Ye, P. Schlottmann, and G. Cao, Ground-state tuning of metal-insulator transition by compositional variations in $BaIr_{1-x}Ru_xO_3$ ($0 \leqslant x \leqslant 1$), Phys. Rev. B **93**, 165136 (2016).

[25] N. A. Bogdanov, V. M. Katukuri, H. Stoll, J. van den Brink, and L. Hozoi, Post-perovskite $CaIrO_3$: A $j = 1/2$ quasi-one-dimensional antiferromagnet, Phys. Rev. B **85**, 235147 (2012).

[26] A. Abragam and B. Bleaney, *Electron Paramagnetic Resonance of Transition Ions* (Clarendon Press, Oxford, 1970).

[27] T. Helgaker, P. Jørgensen, and J. Olsen, *Molecular Electronic-Structure Theory* (Wiley, Chichester, 2000).

[28] A. Berning, M. Schweizer, H.-J. Werner, P. J. Knowles, and P. Palmieri, Spin-orbit matrix elements for internally contracted multireference configuration interaction wavefunctions, Mol. Phys. **98**, 1823 (2000).

[29] H. J. Werner, P. J. Knowles, G. Knizia, F. R. Manby, and M. Schütz, Molpro: a general-purpose quantum chemistry program package, Wiley Rev: Comp. Mol. Sci. **2**, 242 (2012).

[30] J. Pipek and P. G. Mezey, A fast intrinsic localization procedure applicable for *ab initio* and semiempirical linear combination of atomic orbital wave functions, J. Chem. Phys. **90**, 4916 (1989).

[31] Y. Guo, J. Langlois, and W. A. Goddard, Electronic structure and valence-bond band structure of cuprate superconducting materials, Science **239**, 896 (1988).

[32] R. L. Martin and P. W. Saxe, *Ab initio* electronic structure theory for a cluster model of $La_{2-x}Sr_xCuO_4$, Int. J. Quantum Chem. **34**, 237 (1988).

[33] A. B. van Oosten, R. Broer, and W.C. Nieuwpoort, Heisenberg exchange enhancement by orbital relaxation in cuprate compounds, Chem. Phys. Lett. **257**, 207 (1996).

[34] C. J. Calzado, J. Cabrero, J. P. Malrieu, and R. Caballol, Analysis of the magnetic coupling in binuclear complexes. II. Derivation of valence effective Hamiltonians from *ab initio* CI and DFT calculations, J. Chem. Phys. **116**, 3985 (2002).

[35] V. M. Katukuri, V. Yushankhai, L. Siurakshina, J. van den Brink, L. Hozoi, and I. Rousochatzakis, Mechanism of basal-plane antiferromagnetism in the spin-orbit driven iridate Ba_2IrO_4, Phys. Rev. X **4**, 021051 (2014).

[36] S. Nishimoto, V.M. Katukuri, V. Yushankhai, H. Stoll, U. K. Roessler, L. Hozoi, I. Rousochatzakis, and J. van den Brink, Strongly frustrated triangular spin lattice emerging from triplet dimer formation in honeycomb Li_2IrO_3, Nat. Commun. **7**, 10273 (2016).

[37] V. M. Katukuri, S. Nishimoto, I. Rousochatzakis, H. Stoll, J. van den Brink, and L. Hozoi, Strong magnetic frustration and anti-site disorder causing spin-glass behavior in honeycomb Li_2RhO_3, Sci. Rep. **5**, 14718 (2015).

[38] R. Yadav, N. A. Bogdanov, V. M. Katukuri, S. Nishimoto, J. van den Brink, and L. Hozoi, Kitaev exchange and field-induced quantum spin-liquid states in honeycomb $\alpha - RuCl_3$, Sci. Rep. **6**, 37925 (2016).

[39] R. Yadav, M. Pereiro, N. A. Bogdanov, S. Nishimoto, A. Bergman, O. Eriksson, J. van den Brink, and L. Hozoi, Heavy-mass magnetic modes in pyrochlore iridates due to dominant Dzyaloshinskii-Moriya interaction, Phys. Rev. Mater. **2**, 074408 (2018).

[40] R. Yadav, S. Rachel, L. Hozoi, J. van den Brink, and G. Jackeli, Strain- and pressure-tuned magnetic interactions in honeycomb Kitaev materials, Phys. Rev. B **98**, 121107 (2018).

[41] K. I. Kugel, D. I. Khomskii, A. O. Sboychakov, and S. V. Streltsov, Spin-orbital interaction for face-sharing octahedra: Realization of a highly symmetric SU(4) model, Phys. Rev. B **91**, 155125 (2015).

[42] D. I. Khomskii, K. I. Kugel, A. O. Sboychakov, and S. V. Streltsov, Role of local geometry in the spin and orbital structure of transition metal compounds, J. Exp. Theor. Phys. **122**, 484 (2016).

[43] V. M. Katukuri, K. Roszeitis, V. Yushankhai, A. Mitrushchenkov, H. Stoll, M. van Veenendaal, P. Fulde, J. van den Brink, and L. Hozoi, Electronic structure of low-dimensional $4d^5$ oxides: Interplay of ligand distortions, overall lattice anisotropy, and spin-orbit interactions, Inorg. Chem. **53**, 4833 (2014).

[44] L. Hozoi, A. H. de Vries, A. B. van Oosten, R. Broer, J. Cabrero, and C. de Graaf, Theoretical Characterization of the Ground and Optically Excited States of α'-NaV_2O_5, Phys. Rev. Lett. **89**, 076407 (2002).

[45] L. Hozoi, C. Presura, C. de Graaf, and R. Broer, Electronic structure $\alpha' - NaV_2O_5$: Wave-function-based embedded-cluster calculations, Phys. Rev. B **67**, 035117 (2003).

[46] M. Moretti Sala, S. Boseggia, D. F. McMorrow, and G. Monaco, Resonant X-Ray Scattering and the $j_{\text{eff}} = 1/2$ Electronic Ground State in Iridate Perovskites, Phys. Rev. Lett. **112**, 026403 (2014).

[47] G. Bastien, G. Garbarino, R. Yadav, F. J. Martinez-Casado, R. B. Rodríguez, Q. Stahl, M. Kusch, S. P. Limandri, R. Ray, P. Lampen-Kelley, D. G. Mandrus, S. E. Nagler, M. Roslova, A. Isaeva, T. Doert, L. Hozoi, A. U. B. Wolter, B. Büchner, J. Geck, and J. van den Brink, Pressure-induced dimerization and valence bond crystal formation in the Kitaev-Heisenberg magnet α-$RuCl_3$, Phys. Rev. B **97**, 241108 (2018).

[48] S. Sugano, Y. Tanabe, and H. Kamimura, *Multiplets of Transition-Metal Ions in Crystals* (Academic Press, NY & London, 1970).

[49] W. Harrison, *Electonic Structure and the Properties of Solids* (Freeman, San Francisco, 1980).

[50] D. Figgen, K. A. Peterson, M. Dolg, and H. Stoll, Energy-consistent pseudopotentials and correlation consistent basis

sets for the 5*d* elements Hf–Pt, J. Chem. Phys. **130**, 164108 (2009).

[51] K. A. Peterson, D. Figgen, M. Dolg, and H. Stoll, Energy-consistent relativistic pseudopotentials and correlation consistent basis sets for the 4*d* elements Y-Pd, J. Chem. Phys. **126**, 124101 (2007).

[52] T. H. Dunning, Gaussian basis sets for use in correlated molecular calculations. i. the atoms boron through neon and hydrogen, J. Chem. Phys. **90**, 1007 (1989).

[53] I. S. Lim, H. Stoll, and P. Schwerdtfeger, Relativistic small-core energy-consistent pseudopotentials for the alkaline-earth elements from Ca to Ra, J. Chem. Phys. **124**, 034107 (2006).